Chemical Science

ROYAL SOCIETY OF CHEMISTRY

EDGE ARTICLE

View Article Online
View Journal | View Issue

Cite this: *Chem. Sci.*, 2022, **13**, 2640

All publication charges for this article have been paid for by the Royal Society of Chemistry

Unprecedented mid-infrared nonlinear optical materials achieved by crystal structure engineering, a case study of $(KX)P_2S_6$ (X = Sb, Bi, Ba)†

Vivian Nguyen,[a] Bingheng Ji,[a] Kui Wu,[b] Bingbing Zhang *[b] and Jian Wang *[a]

Received 7th December 2021
Accepted 2nd February 2022

DOI: 10.1039/d1sc06849k

rsc.li/chemical-science

Three acentric type-I phase-matchable infrared nonlinear optical materials $KSbP_2S_6$, $KBiP_2S_6$, and $K_2BaP_2S_6$, showing excellent balance between the second harmonic generation coefficient, bandgap, and laser damage threshold, were synthesized *via* a high-temperature solid-state method. $KSbP_2S_6$ is isostructural to $KBiP_2S_6$, which both crystallize in the β-$KSbP_2Se_6$ structure type. $K_2BaP_2S_6$ was discovered for the first time, which crystallizes in a new structure type. $KSbP_2S_6$ and $KBiP_2S_6$ exhibit close structural similarity to the parent compound, centrosymmetric $Ba_2P_2S_6$. The $[P_2S_6]$ motifs, isotypic to ethane, exist in $Ba_2P_2S_6$, $KSbP_2S_6$, $KBiP_2S_6$, and $K_2BaP_2S_6$. The mixed cations, K/Sb pair, K/Bi pair, and K/Ba pair, play a dual-role of aligning the $[P_2S_6]$ structure motifs, contributing to a high SHG coefficient, as well as enlarging the bandgap. $KSbP_2S_6$, $KBiP_2S_6$, and $K_2BaP_2S_6$ are direct bandgap semiconductors with a bandgap of 2.9(1) eV, 2.3(1) eV and 4.1(1) eV, respectively. $KSbP_2S_6$, $KBiP_2S_6$, and $K_2BaP_2S_6$ exhibit a high second harmonic response of 2.2× $AgGaS_2$, 1.8× $AgGaS_2$, and 2.1× $AgGaS_2$, respectively, coupled with a high laser damage threshold of 3× $AgGaS_2$, 3× $AgGaS_2$, and 8× $AgGaS_2$, respectively. The DFT calculations also confirm that the large SHG coefficient mainly originates from $[P_2S_6]$ anionic motifs.

Introduction

Middle infrared lasers have various important applications such as instrumental spectroscopy,[1] optical sensing,[2] optical imaging,[3,4] and long-distance communications.[5] One critical way to obtain middle infrared lasers is *via* the nonlinear harmonic process, where middle infrared nonlinear optical materials (MIR NLO) are the key components. Even after many years of intense research, state-of-the-art MIR NLO materials utilized to cover the spectrum range of 3–25 μm are still underdeveloped. The commercial materials such as $ZnGeP_2$, $AgGaS_2$, and $AgGaSe_2$ are impeded from use in the range of 3–25 μm due to their intrinsic efficiency loss originating from double photon absorption ($ZnGeP_2$), the low laser damage threshold ($AgGaS_2$), and non-phase matchable behavior ($AgGaSe_2$).[6–9] A state-of-the-art MIR NLO should balance a large second harmonic generation coefficient (d_{ij} > $AgGaS_2$), moderate birefringence Δn for phase matchability, a high laser damage threshold (LDT, many times > $AgGaS_2$), and a large bandgap for a good transmission range (>3.5 eV), which is almost impossible for many systems. Many studies, including experimental and theoretical studies, all proved the existence of a "3.5 eV wall" for middle IR NLO.[10–15] Now the major strategy to achieve a large bandgap is through the investigation of oxides, with good examples of $Cs_4V_8O_{22}$,[16] $La_3SnGa_5O_{14}$,[17] $LiCd(IO_3)_3$,[18] Li_2MTeO_6 (M = Ti, Sn),[19] and M_2LiVO_4 (M = Rb, Cs).[20] Compared with oxygen, which has intrinsic vibration modes within the infrared spectrum range, sulfides constituted from heavier sulfur atoms can have better performance.[21–24] For sulfide MIR NLO materials, they currently remain in a vacuum without a promising material to balance d_{ij}, Δn, and LDT with a bandgap breaking through the "3.5 eV wall". A new research strategy is called for to break the "3.5 eV wall" with a good balance of d_{ij}, Δn, and LDT for MIR NLO.

Mixed cations with a combination of two chemically different atoms may increase the structural complexity of the target system, which has a higher chance of forming NCS structures, moderate birefringence for phase-matching behavior, and interactions between cations and anionic groups for better NLO properties.[21,25–30] Our research was firstly inspired by $Ba_2P_2S_6$, which contains $[P_2S_6]$ ethane-like motifs and crystallizes in a centrosymmetric structure.[31] The K^+ cation was selected to replace Ba^{2+} cations due to their comparable ionic sizes: 152 pm and 149 pm, respectively.[32] Trivalent cations containing stereochemically active lone pair electrons (SCALP) such as Sb and Bi were also incorporated into the system. Many previous studies have demonstrated that SCALP play an

[a]*Department of Chemistry and Biochemistry, Wichita State University, Wichita, Kansas, 67260, USA. E-mail: jian.wang@wichita.edu*

[b]*College of Chemistry and Environmental Science, Hebei University, Key Laboratory of Analytical Science and Technology of Hebei Province, Baoding 071002, China*

† Electronic supplementary information (ESI) available: The crystallographic data, powder X-ray diffraction results, Tauc plots, DFT calculation, calculated birefringence, and the calculated SHG intensity map. CCDC 2119928. For ESI and crystallographic data in CIF or other electronic format see DOI: 10.1039/d1sc06849k

important role in enhancing NLO properties.[33–38] Herein, in this study, we verified that a new strategy of applying crystal structure engineering *via* mixed cations plays a dual-role in three emerging MIR NLO materials, $KSbP_2S_6$, $KBiP_2S_6$, and $K_2BaP_2S_6$. The mixed cations, K/Sb, K/Bi and K/Ba, align the $[P_2S_6]$ structure motifs, contributing to both a high SHG coefficient and enlarging the bandgap. The bandgap of $K_2BaP_2S_6$ is 4.1(1) eV, which sets a new record for superior MIR NLO sulfide materials. $KSbP_2S_6$, $KBiP_2S_6$, and $K_2BaP_2S_6$ are all type-I phase-matchable materials with very large bandgaps (2.9(1) eV, 2.3(1) eV, and 4.1(1) eV, respectively), high SHG coefficients (2.2× $AgGaS_2$, 1.8× $AgGaS_2$, and 2.1× $AgGaS_2$, respectively) and large LDT (3× $AgGaS_2$, 3× $AgGaS_2$, and 8× $AgGaS_2$, respectively). The structural chemistry between $KSbP_2S_6$, $KBiP_2S_6$, $K_2BaP_2S_6$, and the parent centrosymmetric compound $Ba_2P_2S_6$ [31] is presented. The synthesis, crystal structure, electronic structure, linear and nonlinear optical properties, and DFT calculations of $KSbP_2S_6$, $KBiP_2S_6$, and $K_2BaP_2S_6$ and the parent centrosymmetric compound $Ba_2P_2S_6$ are discussed.

Experimental

Synthesis

All starting materials were stored and used in an Ar-filled glove box. Starting materials were used as received without further handling: K metal (Alfa Aesar, 99.95%), P powder (Alfa Aesar, 99.5%), S powder (Alfa Aesar, 99.5%), Ba rod (Sigma-Aldrich 99.9%), Bi (Fisher, 99.99%), and Sb (Fisher, 99.5%). The P_2S_5 precursor was made *via* loading P and S at a molar ratio of 2 : 5 and heating them to 573 K in 10 hours and holding for 10 hours. Polycrystalline samples of $K_2BaP_2S_6$, $KSbP_2S_6$, and $KBiP_2S_6$ were grown by a two-step solid-state reaction. First step: stoichiometric amounts of reactants ($K_2BaP_2S_6$: K/Ba/P/S = 2 : 1 : 2 : 6, $KSbP_2S_6$: K/Sb/P/S = 1 : 1 : 2 : 6, $KBiP_2S_6$: K/Bi/P/S = 1 : 1 : 2 : 6) were loaded into silica quartz tubes and were flame-sealed under vacuum at 10^{-2} torr and placed into a programmable furnace. The sealed silica tubes were heated to 398 K in 10 h, held for 10 h, heated to 923 K in 10 h, held for 144 h, and cooled to RT over 48 h. Second step: the quartz tubes from the first step were opened in a glovebox and the products were manually ground using a mortar and pestle. The finely mixed powders were then loaded into a new carbonized quartz tube. The ampoules were sealed and heated again using an identical temperature profile to the first step. After the second step, the homogeneous powders appearing in various colors ($K_2BaP_2S_6$: white transparent, $KSbP_2S_6$: yellow-green, $KBiP_2S_6$: red) were collected and checked by powder X-ray diffraction. The powder X-ray diffraction verified the single-phase nature of $K_2BaP_2S_6$, $KSbP_2S_6$, and $KBiP_2S_6$ (Fig. S1–S3†).

Single crystal X-ray diffraction

X-ray diffraction data were collected at 298(2) K for $K_2BaP_2S_6$ using a Bruker Kappa APEX II diffractometer with graphite monochromated Mo Kα radiation (λ = 0.71073 Å). Data reduction and integration, together with global unit cell refinements, were performed in the APEX2 software.[39] Multi-scan absorption corrections were employed.[39] The structures were solved by direct methods and refined by full matrix least-squares methods on F^2 using the SHELX package with anisotropic displacement parameters for all atoms.[40] In the last refinement cycles, the atomic positions for the three compounds were standardized using the program structure TIDY.[41,42] Details of the data collection and structure refinement are provided in Table 1. Atomic coordinates and selected bond distances are summarized in Tables S1 and S2.† During the structure refinement process, a residual peak separated from the K2 atom by 2.87(2) Å with an intensity of 5.22 e $Å^{-3}$ was found in $K_2BaP_2S_6$. The final refinement ended up with a high wR_2 of 0.1458 ([$I > 2\sigma(I)$]) and G.O.F of 1.200. The twinning refinement and reproduced data collection with better crystal quality did not improve the refinement results. With defining the residual peak as K1 with adding constraints of occupancy of K1 + K2 = 100%, the final structure model ended up with a much lower wR_2 of 0.0807 ([$I > 2\sigma_{(I)}$]), wR_2 of 0.0874 (all data), and G.O.F of 1.071. When solely refining the occupancy of K2, a value of 97% was obtained. The occupancy of interstitial K1 is around 13% from single crystal refinement results. Since $K_2BaP_2S_6$ was revealed as a large bandgap semiconductor by theoretical simulation and experimental UV-vis results (*vide infra*), the charge-balanced formula $(K^+)_2(Ba^{2+})(P^{4+})_2(S^{2-})_6$ can be established by assigning a formal charge of 1+ to the K atoms, 2+ to the Ba atoms, 4+ to the P atoms due to the presence of homoatomic interactions, and 2− to the S atoms. Hence, the actual occupancy of interstitial K1 would be much lower than 10% to keep the charge balanced nature of $K_2BaP_2S_6$. To simplify the discussion of $K_2BaP_2S_6$, the interstitial K1 was not included. The crystallographic data such as atomic coordinate parameters and selected interatomic distances of K1 atoms are listed in Tables S1 and S2,† respectively. Crystallographic data for $K_2BaP_2S_6$ have been deposited with the Cambridge Crystallographic Data Centre, CCDC, 12 Union Road, Cambridge CB21EZ, UK. Copies of the data can be obtained free of charge on quoting the depository number CCDC-2119928 ($K_2BaP_2S_6$).

Powder X-ray diffraction

Data were collected at room temperature using a Rigaku Mini Flex II diffractometer with Cu Kα radiation (λ = 1.5406 Å).

UV-vis measurements

Diffuse-reflectance spectra were recorded at room temperature using a PERSEE-T8DCS UV-vis spectrophotometer equipped with an integration sphere in the wavelength range of 230–850 nm. The reflectance data, R were recorded and converted to the Kubelka–Munk function, $f(R) = (1 - R)^2(2R)^{-1}$. The Tauc plots, $(KM \times E)^2$ and $(KM \times E)^{1/2}$, were applied to estimate direct and indirect bandgaps, respectively.

Second harmonic measurements

Using the Kurtz and Perry method,[43] powder SHG responses of title compounds were investigated using a Q-switch laser (2.09 μm, 3 Hz, 50 ns) with different particle sizes, including 38.5–54, 54–88, 88–105, 105–150, and 150–200 μm. The detailed process

Table 1 Selected crystal data and structure refinement parameters for $K_2BaP_2S_6$ at 173(2) K

Empirical formula	$K_2BaP_2S_6$		
Formula weight	469.84 g mol^{-1}	Unit cell volume	1211.8(2) Å^3
Temperature	173(2) K	Z	4
Radiation, wavelength	Mo Kα, 0.71073 Å	Density (calc.)	2.575 g cm^{-3}
Crystal system	Orthorhombic	Absorption coefficient	5.203 mm^{-1}
Space group	$Pna2_1$ (no. 33)		
Unit cell dimensions	a = 12.3592(13) Å	Final R indices[a] [$I > 2\sigma_{(I)}$]	R_1 = 0.0373
			wR_2 = 0.0807
	b = 14.4324(14) Å	Final R indices[a] [all data]	R_1 = 0.0561
			wR_2 = 0.0874
	c = 6.7939(7) Å	G.O.F	1.071

[a] $R_1 = \sum||F_o| - |F_c||/\sum|F_o|$; w$R_2 = [\sum[w(F_o^2 - F_c^2)^2]/\sum[w(F_o^2)^2]]^{1/2}$, and $w = 1/[\sigma^2F_o^2 + (A\cdot P)^2 + B\cdot P]$, $P = (F_o^2 + 2F_c^2)/3$; A and B are weight coefficients.

of sample preparation would be: the as-synthesized sample and the as-synthesized reference $AgGaS_2$ sample were manually ground into particles within a glovebox first. The ground samples were sieved using standard brass sieves with various mesh sizes. The particles were sorted out and separated using standard brass sieves with various mesh sizes with the potential of a large range of particle size distribution. The LDTs of the title compounds were evaluated on powder samples (150–200 μm) with a pulsed YAG laser (1.06 μm, 10 ns, 10 Hz). The judgment criterion is as follows: with increasing laser energy, the color change of the powder sample is constantly observed using an optical microscope to determine the damage threshold. To adjust different laser beams, an optical concave lens is added to the laser path. The damaged spot is measured using the scale of the optical microscope.

Theoretical calculations

The density of states (DOS), partial density of states (PDOS), band structure, crystal orbital Hamilton population (COHP), and electron localization function (ELF) of $Ba_2P_2S_6$, $KBiP_2S_6$, and $K_2BaP_2S_6$ are calculated using the tight binding-linear muffin tin orbitals-atomic sphere approximation (TB-LMTO-ASA) program.[44,45] The Barth–Hedin exchange potential was employed for the LDA calculations.[45] The radial scalar-relativistic Dirac equation was solved to obtain the partial waves. The basis set used contained K (4s), Ba (6s, 5d, 4f), Bi (6s, 5d, 6p), P (3s, 3p) and S (3s, 3p) orbitals, and was employed for a self-consistent calculation, with downfolded functions of K (4p, 3d), Ba (5f, 6p), Bi (6d, 5f), P (3d) and S (3d). The density of states and band structures were calculated after converging the total energy on a dense k-mesh of $Ba_2P_2S_6$ (20 × 20 × 10 points with 1122 irreducible k-points), $K_2BaP_2S_6$ (12 × 12 × 24 points with 1176 irreducible k-points), and $KBiP_2S_6$ (16 × 16 × 8 points with 1056 irreducible k-points). The optical properties were calculated based on *ab initio* calculations implemented in the CASTEP package through density functional theory (DFT).[46] The generalized gradient approximation (GGA)[47] was adopted, and the Perdew–Burke–Ernzerhof (PBE)[48] function was chosen to calculate the exchange–correlation potential, with an energy cutoff of 650 eV. The numerical integration of the Brillouin zone was performed using Monkhorst–Pack k-point sampling. The k-point separation for each material was set as 0.04 Å^{-1}. The geometry optimizations were applied prior to property calculations. Norm-conserving pseudopotentials were employed.

Results and discussion

Crystal structure

$KSbP_2S_6$ is isostructural to $KBiP_2S_6$, which crystallizes in the β-$KSbP_2Se_6$ structure type.[49] $KSbP_2S_6$ and $KBiP_2S_6$ form in the monoclinic space group $P2_1$ (no. 4), which were discovered by Manrique, V. *et al.* without investigating any properties.[50] $K_2BaP_2S_6$ crystallizes in the orthorhombic space group $Pna2_1$ (no. 33) with unit cell parameters of a = 12.018(1) Å, b = 23.762(2) Å, and c = 3.984(1) Å. The Wyckoff sequence of $K_2BaP_2S_6$ is a^{11} with Pearson symbol $oP44$. Searching for isostructural compounds through the ICSD database did not return any results. Therefore, $K_2BaP_2S_6$ crystallizes in a new structure type. The selected crystal data and structure refinement parameters for $K_2BaP_2S_6$ are summarized in Table 1. The atomic coordinate parameters and selected interatomic distances are listed in Tables S1 and S2.†

To discuss the structural chemistry between $KSbP_2S_6$, $KBiP_2S_6$, and $K_2BaP_2S_6$, a centrosymmetric compound $Ba_2P_2S_6$ [31] must be discussed for a few reasons: (1) the fundamental building units of $Ba_2P_2S_6$ are the $[P_2S_6]$ motifs, which are the same fundamental building units in $KSbP_2S_6$, $KBiP_2S_6$, and $K_2BaP_2S_6$; (2) there are close unit cell parameters between $Ba_2P_2S_6$, $KSbP_2S_6$, and $KBiP_2S_6$ with very comparable unit cell volumes as shown in Table S3;† (3) the chemical formula of $Ba_2P_2S_6$ can be presented by $[Ba^{2+}]_2[P_2S_6]^{4-}$, where the charge of cations would be 4+. The same charge requirements remain in $KSbP_2S_6$, $KBiP_2S_6$, and $K_2BaP_2S_6$ with representation as $[K^+Sb^{3+}][P_2S_6]^{4-}$, $[K^+Bi^{3+}][P_2S_6]^{4-}$, and $[K_2{}^+Ba^{2+}][P_2S_6]^{4-}$ respectively; (4) $Ba_2P_2S_6$ inspired our research interest in compounds containing $[P_2S_6]$ motifs. Since $KSbP_2S_6$ is isostructural to $KBiP_2S_6$, only $KBiP_2S_6$ is selected for structural discussion. The structural comparisons between centrosymmetric $Ba_2P_2S_6$, $KSbP_2S_6$, and $K_2BaP_2S_6$ are summarized in Fig. 1 with emphasis on the $[P_2S_6]$ motifs on the right.

$Ba_2P_2S_6$ crystallizes in the centrosymmetric $P2_1/n$ (no. 14) space group with unit cell parameters of a = 6.7459(6) Å, b =

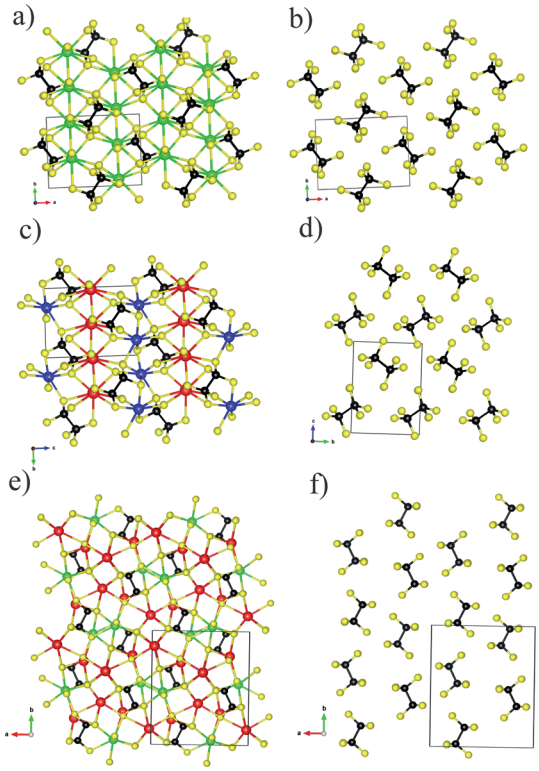

Fig. 1 (a) Ball-stick structure model of $Ba_2P_2S_6$ viewed along the [001] axis, (b) the arrangement of $[P_2S_6]$ motifs within $Ba_2P_2S_6$. (c) Ball-stick structure model of $KBiP_2S_6$ viewed along the [100] axis, (d) the arrangement of $[P_2S_6]$ motifs within $KBiP_2S_6$. (e) Ball-stick structure model of $K_2BaP_2S_6$ viewed along the [001] axis, (f) the arrangement of $[P_2S_6]$ motifs within $K_2BaP_2S_6$. K red color, Ba: green color, Bi: blue color, P: black color, S: yellow color.

7.5871(6) Å, and c = 9.9983(9) Å, β = 91.204(3)°, which were redetermined in this work. The crystal structure of $Ba_2P_2S_6$ is shown in Fig. 1a and b. The three-dimensional (3D) framework of $Ba_2P_2S_6$ is constructed by isolated $[P_2S_6]$ motifs interconnected by 2D $[Ba_2S_6]$ slabs, where the center Ba atoms are surrounded by nine sulfur atoms. The Ba–S interactions within $[BaS_9]$ polyhedra fall into the range of 3.217–3.567 Å. The theoretical simulation also verified the ionic bonding nature of Ba–S interactions (*vide infra*). The crystal structure of $KBiP_2S_6$ shows high similarity to $Ba_2P_2S_6$, as summarized in Table S3† and Fig. 1. $KBiP_2S_6$ crystallizes in the acentric $P2_1$ (no. 4) space group with unit cell parameters of a = 6.6200(6) Å, b = 7.4058(7) Å, and c = 9.9002(9) Å, β = 92.108(1) °.[50] The unit cell volume of $Ba_2P_2S_6$ and $KBiP_2S_6$ is 508.82 Å^3 and 485.04 Å^3, respectively. The 3D framework of $KBiP_2S_6$ is formed by isolated $[P_2S_6]$ motifs linked by alternatively arranged 2D $[KS_5]$ slabs and 2D $[BiS_5]$ slabs, which are shown in Fig. 1c. The 2D $[KS_5]$ slabs are constructed by $[KS_9]$ polyhedra interlinked *via* sharing vertices and edges. The K–S interactions within $[KS_9]$ polyhedra are 3.191–3.592 Å, comparable to Ba–S interactions of 3.217–3.567 Å within $Ba_2P_2S_6$, which are revealed as dominantly ionic bonds (*vide infra*). The 2D $[BiS_5]$ slabs are made by distorted $[BiS_7]$ polyhedra with Bi–S interactions of 2.706–3.210 Å. The Bi–S interactions of 2.71 Å show strong polarized ionic bonding characteristics (*vide infra*).

$K_2BaP_2S_6$ exhibits a much more complex structure than $Ba_2P_2S_6$ and $KBiP_2P_6$. $K_2BaP_2S_6$ crystallizes in the orthorhombic space group $Pna2_1$ (no. 33) with unit cell parameters of a = 12.3592(13) Å, b = 14.4324(14) Å, and c = 6.7939(7) Å with unit cell volume of 1211.8(2) Å^3, about two times higher than those of $Ba_2P_2S_6$ (508.82 Å^3) and $KBiP_2P_6$ (485.04 Å^3). The 3D framework of $K_2BaP_2S_6$ can be viewed as isolated $[P_2S_6]$ motifs connected by 2D $[K_2BaS_6]$ slabs, where the K/Ba ratio is two. The 2D $[K_2BaS_6]$ slabs are made of $[KS_7]$ polyhedra, $[KS_8]$ polyhedra, and $[BaS_{10}]$ polyhedra. The K–S interactions in $[KS_7]$ and $[KS_8]$ fall into the range of 3.213(16)–3.679(5) Å, which is close to those of many potassium-sulfides such as $K_2FeGe_3S_8$ (3.131–3.762 Å),[51] $K_2CoGe_3S_8$ (3.130–3.765 Å),[51] $KBiP_2S_6$ (3.191–3.562 Å),[50] $K_2MnP_2S_6$ (3.226–3.600 Å),[52] $KSbP_2S_6$ (3.206–3.592 Å).[50] The 3.220(5) Å K–S interactions are revealed by theoretical calculations as weak ionic bonds (*vide infra*). The Ba–S interactions in $[BaS_{10}]$ polyhedra fall into the range of 3.226(3)–3.535(7) Å, which is close to those of many barium-sulfides such as $Ba_6(Cu_2Mg)Ge_4S_{16}$ (3.084–3.454 Å),[53] $Ba_2P_2S_6$ (3.217–3.567 Å),[31] Ba_2AlSbS_5 (3.217–3.567 Å),[54] $BaAg_2GeS_4$ (3.251–3.306 Å),[55] $BaCd_2As_2S_6$ (3.248–3.374 Å),[56] *etc.* The 3.24 Å ionic Ba–S interactions exhibit certain bond strengths as revealed by theoretical calculations (*vide infra*). The structural details of $K_2BaP_2S_6$ are shown in Fig. 1e and f. The $[P_2S_6]$ motifs are the common features existing in $Ba_2P_2S_6$, $KBiP_2P_6$ and $K_2BaP_2S_6$. The $[P_2S_6]$ motif is isotypic to ethane, constructed by a P–P dimer with three sulfur atoms surrounding each P atom. The interatomic P–P bonds for $Ba_2P_2S_6$, $KBiP_2P_6$ and $K_2BaP_2S_6$ are 2.205 Å, 2.219 Å, and 2.223(4) Å, respectively, which are typical for homoatomic P–P bond distances such as $BaCu_5P_3$ (2.263 Å),[57] $La_2Ba_6Cu_{16}P_{30}$ (2.071–2.428 Å),[58] $BaCu_2P_4$ (2.183 and 2.289 Å),[59] $Ba_8Cu_{16}P_{30}$ (2.159–2.299 Å),[60] $La_7Zn_2P_{11}$ (2.207(7) Å),[61] $Ba_2Cu_3P_4$ (2.236 Å),[62] $La_4Zn_7P_{10}$ (2.151(8) Å),[63] *etc.* The P–S interatomic distances within $Ba_2P_2S_6$ are 2.016–2.025 Å, and are slightly expanded into a wider range of distances to 1.962–2.057 Å and 1.958(17)–2.066(15) Å for $KBiP_2P_6$ and $K_2BaP_2S_6$, respectively. Even though all $[P_2S_6]$ motifs have identical geometry within $Ba_2P_2S_6$, $KBiP_2P_6$, and $K_2BaP_2S_6$, the slightly different interatomic distances coupled with various ∠S–P–S angles indicate that the degrees of distortion of the $[P_2S_6]$ motifs are distinct. The strong covalent bonding nature of P–P interactions and P–S interactions together with complex interactions between cations and $[P_2S_6]$ was uncovered by theoretical simulation (*vide infra*).

Another intriguing structural feature of $Ba_2P_2S_6$, $KBiP_2P_6$ and $K_2BaP_2S_6$ is the arrangement of $[P_2S_6]$ motifs as shown in Fig. 1b, d and f. To discuss the alignment of $[P_2S_6]$ motifs, we introduce the ∠P–P–P angles as a measure, where the three P atoms are coming from two neighbor $[P_2S_6]$ motifs. The ∠P–P–P angles are summarized in Table 2. From Table 2, the ∠P–P–P

Table 2 The comparison of ∠P–P–P angles between $Ba_2P_2S_6$, $KBiP_2S_6$, and $K_2BaP_2S_6$

	$Ba_2P_2S_6$	$KbiP_2S_6$	$K_2BaP_2S_6$
∠P–P–P/°	70.53(4)	73.57(3)	89.4(3)

angle significantly increases from $Ba_2P_2S_6$ to $K_2BaP_2S_6$ of 70.73(4)° and 89.4(3)° respectively. The ∠P–P–P angle in $KBiP_2S_6$ resides between $Ba_2P_2S_6$ and $K_2BaP_2S_6$ of 73.57(3)°. The ∠P–P–P angle is closer to 90°, which indicates that $[P_2S_6]$ motifs are arranged more parallel to each other. As shown in Fig. 1f, the $[P_2S_6]$ motifs within $K_2BaP_2S_6$ are arranged nearly parallel. The later studies demonstrate that the alignment of $[P_2S_6]$ motifs is crucial for the optical properties of $K_2BaP_2S_6$ (*vide infra*).

Electronic structures

To elucidate the electronic structures of $Ba_2P_2S_6$, $KBiP_2S_6$, and $K_2BaP_2S_6$, the calculations of band structure and density of states (DOS) were employed. The band structures are summarized in Fig. S4–S11.† The density of states of $Ba_2P_2S_6$, $KBiP_2S_6$, and $K_2BaP_2S_6$ is shown in Fig. 2. To validate the accuracy of theoretical simulations, two different methods, TB-LMTO-ASA and VASP, were employed to study the electronic structures of $Ba_2P_2S_6$, $KBiP_2S_6$, and $K_2BaP_2S_6$ (Fig. 2 and S4–S14†), which exhibited comparable results.

The charge-balanced formula $(Ba^{2+})_2(P^{4+})_2(S^{2-})_6$, $(K^{1+})(Bi^{3+})(P^{4+})_2(S^{2-})_6$, and $(K^{1+})_2(Ba^{2+})(P^{4+})_2(S^{2-})_6$ can be easily achieved *via* assigning a formal charge of 2+ to the Ba atoms, 1+ to the K atoms, 3+ to the Bi atoms, 4+ to the P atoms due to the presence of P–P homoatomic bonds, and 2− to the S atoms. The Bi^{3+} is confirmed by the presence of $6p^2$ lone pair electrons elucidated by ELF calculations (*vide infra*) and bond valence sum calculations.[64–66] Bond valence sum calculations indicated that the BVS of K atoms, Ba atoms and Bi atoms is 1.1, 1.9, and 2.5, respectively, which suggests K atoms, Ba atoms and Bi atoms with oxidation states of +1, +2, and +3, respectively. The semiconductor nature of $Ba_2P_2S_6$, $KBiP_2S_6$, and $K_2BaP_2S_6$ was verified by DFT calculations and UV-vis measurements (Fig. S15–S19†). The band structure calculation indicated the direct semiconductor nature of $Ba_2P_2S_6$, $KBiP_2S_6$, and $K_2BaP_2S_6$ (Fig. S6, S7, S9 and S10†). As shown in Fig. 2 left, the calculated bandgap of $Ba_2P_2S_6$ is 3.3 eV, which is lower than the measured value of 4.3(1) eV (Fig. S15 and S16†). In $Ba_2P_2S_6$, the top of the valence band is dominantly contributed by S 3p orbitals and Ba 5s orbitals with some contributions from P 3p orbitals. The bottom of the conduction band is mainly contributed by S 3p orbitals and P 3p orbitals with certain contribution from Ba orbitals. The Ba orbitals significantly contribute a high energy interval of 5–7 eV as shown on the left of Fig. 2. We can anticipate that the Ba–S interactions are crucial for enlarging the bandgap of $Ba_2P_2S_6$ and the optical properties of $Ba_2P_2S_6$ are mainly controlled by Ba–S interactions and P–S interactions.

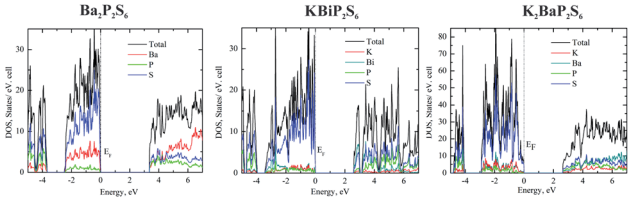

Fig. 2 Left: density of states of $Ba_2P_2S_6$, middle: density of states of $KBiP_2S_6$, right: density of states of $K_2BaP_2S_6$.

The direct bandgap of $KBiP_2S_6$ was predicated to be 2.6 eV, which is slightly higher than the measured value of 2.3(1) eV (Fig. S18†). The HSE calculated bandgap is 2.37 eV, which agrees very well with the measured value (Fig. S7†). $KBiP_2S_6$ exhibits a comparable electronic structure to $Ba_2P_2S_6$, which is shown in the middle of Fig. 2. The top of the valence band is mainly contributed by S 3p orbitals with almost equal contributions from K 4s orbitals, Bi 6p orbitals and P 3p orbitals. The bottom of the conduction band is dominantly contributed by Bi 6p orbitals and S 3p orbitals with significant contribution from P 3p orbitals. Interestingly, K 4s orbitals had a negligible contribution to the bottom of the conduction band. Compared with $Ba_2P_2S_6$, $[BiS_7]$ polyhedra will be expected to significantly affect the optical properties of $KBiP_2S_6$, which was verified by DFT calculations (*vide infra*). The nonlinear optical process is mainly dominated by electrons transferring between these frontier orbitals. Within $KBiP_2S_6$, K–S interactions, Bi–S interactions and $[P_2S_6]$ motifs all determine the optical properties of $KBiP_2S_6$. The stereochemically active lone pair electrons (SCALP) on Bi atoms are expected to significantly enhance the NLO properties of $KBiP_2S_6$, which is confirmed by experimental observations and DFT calculations (*vide infra*). Compared with the centrosymmetric $Ba_2P_2S_6$, the mixed cations of K/Bi play a dual-role of shifting the arrangement of $[P_2S_6]$ to form a NCS structure and shrinking the bandgap.

The dual-role of mixed cations is even more obvious in $K_2BaP_2S_6$. The direct bandgap of $K_2BaP_2S_6$ was predicated to be 2.6 eV and 2.5 eV by the tight bonding method and HSE calculation respectively (Fig. S9 and S10†). The experimentally measured bandgap of $K_2BaP_2S_6$ is 4.1(1) eV, where the underestimation of the bandgap is normal for DFT calculations. The electronic structures of $K_2BaP_2S_6$ exhibit certain high similarity to $Ba_2P_2S_6$ and $KBiP_2S_6$. The top of the valence band is predominantly contributed by S 3p orbitals and small contents of contribution from K 4s orbitals and Ba 6s orbitals. The contribution from P 3p orbitals can be ignored at the top of the valence band. Inversely, the P 3p orbitals coupled with S 3p orbitals and Ba 6s orbitals dominantly contribute to the bottom of the conduction band, where K 4s orbitals have certain contributions. From the density of states, we can expect that $[P_2S_6]$ motifs significantly shift the nonlinear optical properties of $K_2BaP_2S_6$, while mixed cations of K/Ba forming ionic K–S interactions and Ba–S interactions are responsible for the large bandgap of $K_2BaP_2S_6$. In addition to enlarging the bandgap of $K_2BaP_2S_6$, mixed cations of K/Ba also account for the nearly parallel alignment of $[P_2S_6]$ motifs, which is crucial for its superior optical performance (*vide infra*).

Bonding picture studies

The bonding pictures of $Ba_2P_2S_6$ (Fig. 3a and b), $KBiP_2S_6$ (Fig. 3c and d), and $K_2BaP_2S_6$ (Fig. 3e and f) were understood with the aid of the electron localization function (ELF) coupled with crystal orbital Hamilton population (COHP) calculations. For $Ba_2P_2S_6$, there are no detectable attractors (ELF maxima

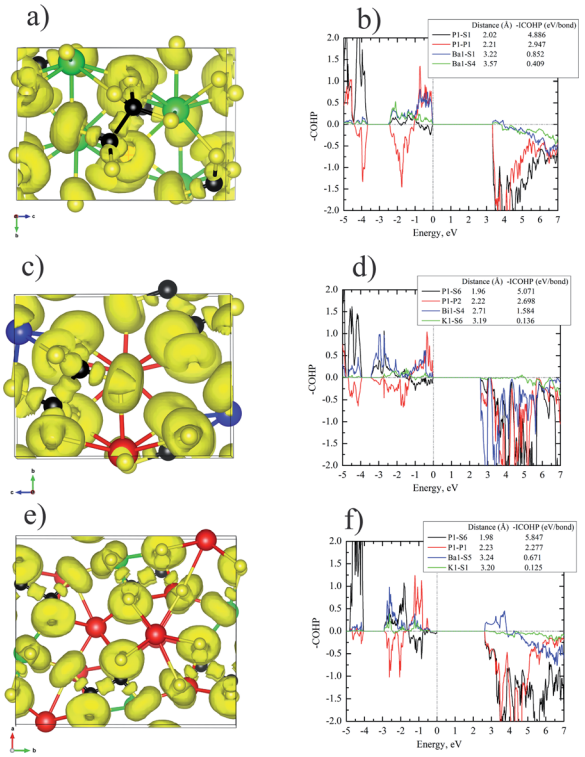

Fig. 3 (a, c and e) 3D isosurfaces of the electron localization function (ELF) for $Ba_2P_2S_6$ (a), $KBiP_2S_6$ (c), and $K_2BaP_2S_6$ (e) with $\eta = 0.75$, Ba: green color, K: red color, Bi: blue color, P: Black color, S: yellow color, (b, d and f): Crystal Orbital Hamilton Population (COHP) analyses of the selected interactions within $Ba_2P_2S_6$ (b), $KBiP_2S_6$ (d), and $K_2BaP_2S_6$ (f).

isosurfaces) found between Ba–S interactions with attractors only surrounding S atoms, which suggests the dominant ionic character of Ba–S interactions. The Ba–S interactions exhibit certain strong bonding characteristics with –ICOHPs of 0.852 eV per bond and 0.409 eV per bond for 3.22 Å Ba–S interactions and 3.57 Å Ba–S interactions, respectively. An obvious attractor was located between P–P interactions with –ICOHPs of 2.947 eV per bond for 2.21 Å P–P interactions, which indicates the strong covalent bonding nature of P–P interactions. The strongest bonding character was found between P–S interactions. The –ICOHPs for 2.02 Å P–S interactions are 4.886 eV per bond. There were significant attractors located between P–S bonds with a small shift toward P atoms. All attractors surrounding S atoms show irregular spherical shapes, which indicates the polarized bonding nature of Ba–S interactions and P–S interactions. For $KBiP_2S_6$, K atoms play the role of cations with no attractors surrounding and existing between K–S interactions and low calculated –ICOHPs of 0.136 eV per bond for 3.19 Å K–S interactions, which demonstrates the weak ionic bonding nature of K–S interactions. The attractors capping the Bi atoms correspond to the $6s^2$ electron lone pairs on Bi atoms, which verifies that the oxidation states of Bi should be +3. The COHP calculations indicate the strong bonding interactions for 2.71 Å Bi–S bonding with –ICOHPs of 1.584 eV per bond. For Bi–S interactions, the attractors are solely surrounding S atoms with irregular shapes, which suggests the strong polarized dominantly ionic bonding characters of Bi–S interactions. The electronic studies predict that $[BiS_7]$ polyhedra will significantly contribute to NLO properties due to the presence of SCALP, which is confirmed by DFT calculations (*vide infra*). The P–P interactions and P–S interactions within $KBiP_2S_6$ exhibit comparable characters to $Ba_2P_2S_6$. There are attractors located in the middle of P–P interactions with –ICOHPs of 2.698 eV per bond for 2.22 Å P–P interactions. There are attractors detected between P–S interactions with –ICOHPs of 5.071 eV per bond for 1.96 Å P–S interactions. Hence, both P–P interactions and P–S interactions exhibit strong covalent bonding characteristics.

For $K_2BaP_2S_6$, there are no ELF maxima isosurfaces residing between K–S interactions and Ba–S interactions. The calculated –ICOHPs for 3.24 Å Ba–S interactions are 0.671 eV per bond, which indicates that 3.24 Å Ba–S has certain strong bonding characteristics. The 3.20 Å K–S interactions have much weaker ionic bonding nature with –ICOHPs of 0.125 eV per bond as shown in Fig. 3f. The electronegativity difference between K (0.8) and Ba (0.9) may account for this slight bonding picture difference. The strong covalent bonding nature of P–P interactions and P–S interactions was verified by the presence of attractors between them and high –ICOHPs values of 5.847 eV per bond and 2.277 eV per bond for 1.98 Å P–S bonds and 2.23 Å P–P bonds, respectively. Similar to $Ba_2P_2S_6$ and $KBiP_2S_6$, the K–S interactions and Ba–S interactions are also strongly polarized. When comparing $Ba_2P_2S_6$, $KBiP_2S_6$, and $K_2BaP_2S_6$ together, one very interesting observation is the decrease of bonding strengths in P–P interactions and the inverse trend of enhancement of bonding strengths in P–S interactions from $Ba_2P_2S_6$ to $KBiP_2S_6$, and finally to $K_2BaP_2S_6$. All our observations indicate the complex interactions happening between cations and anionic $[P_2S_6]$ motifs.

Linear and nonlinear optical properties

The linear and nonlinear optical properties of $KSbP_2S_6$, $KBiP_2S_6$, and $K_2BaP_2S_6$ were measured and are reported in Fig. 4. From Fig. 4a, $Ba_2P_2S_6$, $KBiP_2S_6$, and $K_2BaP_2S_6$ exhibited type-I phase-matching behavior, where the SHG response increases with particle size increasing. The calculated birefringence of $KSbP_2S_6$, $KBiP_2S_6$, and $K_2BaP_2S_6$ is shown in Fig. S12–S14.† The

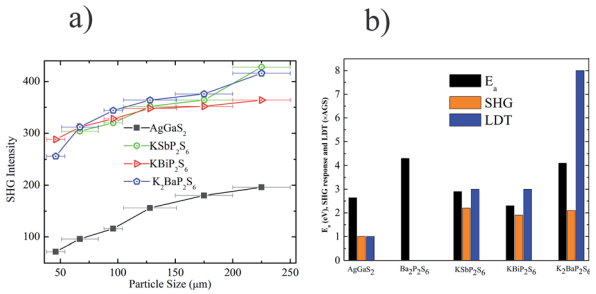

Fig. 4 (a) SHG intensities of $Ba_2P_2S_6$, $KBiP_2S_6$, $K_2BaP_2S_6$, and $AgGaS_2$ were measured on variable particle size samples utilizing a 2.09 μm laser. (b) The comparison of the bandgap (Ea), SHG response (×$AgGaS_2$ based on 225 μm particle size samples) and LDT (×$AgGaS_2$) between $Ba_2P_2S_6$, $KBiP_2S_6$, $K_2BaP_2S_6$, and $AgGaS_2$.

moderate birefringence of $KSbP_2S_6$, $KBiP_2S_6$, and $K_2BaP_2S_6$ accounts for their phase-matching capability, which is crucial for practical applications. For samples of particle size 225 μm, the SHG response of $KSbP_2S_6$, $KBiP_2S_6$, and $K_2BaP_2S_6$ is 2.2× AGS, 1.8× AGS and 2.1× AGS, respectively. The measured bandgap of $KSbP_2S_6$, $KBiP_2S_6$, and $K_2BaP_2S_6$ is 2.9(1) eV, 2.3(1) eV and 4.1(1) eV respectively. The high bandgap of $K_2BaP_2S_6$ results in an extraordinarily high LDT of 8× AGS. $KSbP_2S_6$ and $KBiP_2S_6$ also possess excellent LDT of about 3× AGS for both samples. The type-I phase matching behavior, large bandgap, high SHG response, and high LDT make $KSbP_2S_6$, $KBiP_2S_6$, and especially $K_2BaP_2S_6$ ideal candidates for middle IR NLO applications.

DFT calculations

To better understand the origin of the superior NLO properties of $KSbP_2S_6$, $KBiP_2S_6$ and $K_2BaP_2S_6$, DFT calculations were carried out and are summarized in Table 3, Fig. 5 and S20–S22.† The calculations of $KSbP_2S_6$ are presented in Fig. S20.† As shown in Table 3, $KSbP_2S_6$ and $KBiP_2S_6$ were predicated to show a high SHG response, which agrees well with our experimental observations. The calculated χ^{222} for $KSbP_2S_6$ is 67.267 pm V^{-1} which is slightly higher than that of $KBiP_2S_6$ at $\chi^{222} = 63.404$ pm V^{-1}. The experimentally measured SHG response of $KSbP_2S_6$ is also slightly better than that of $KBiP_2S_6$. From Fig. 5a and b, the occupied virtual electrons (VE) states of $KSbP_2S_6$ and $KBiP_2S_6$ are mainly contributed by the $[P_2S_6]$ motif and $[XS_7]$ (X = Sb or Bi) polyhedra due to the presence of SCALP, which is verified by the analysis of unoccupied virtual electrons states and virtual holes (VH) (Fig. S20 and S21†). These observations agree well with our previous electronic structure analysis.

For $K_2BaP_2S_6$, the analysis of occupied and unoccupied states of VE and VH concluded that the $[P_2S_6]$ motif plays a critical role in determining the SHG response, which agrees well with our electronic structure study. The calculated χ^{333} of $K_2BaP_2S_6$ is only around 0.678 pm V^{-1}, which is much lower than that of $KSbP_2S_6$ and $KBiP_2S_6$. The experimentally measured SHG response of $K_2BaP_2S_6$ is comparable to that of $KSbP_2S_6$ and slightly better than that of $KBiP_2S_6$. This controversy can be explained by the alignment of $[P_2S_6]$ motifs, as discussed in the crystal structure analysis. The nearly parallel alignment of $[P_2S_6]$ motifs guarantees that the dipole moments originating from the $[P_2S_6]$ motif do not cancel each other out during the nonlinear polarization process.[67,68] For $KSbP_2S_6$ and $KBiP_2S_6$, the "imperfect" alignment of $[P_2S_6]$ motifs is compensated by the presence of SCALP, which also results in a superior SHG response. In summary, $K_2BaP_2S_6$ exhibits an excellent example

Table 3 Calculated second-order nonlinear susceptibility χ^{abc} for $KSbP_2S_6$, $KBiP_2S_6$, and $K_2BaP_2S_6$

	$KSbP_2S_6$	$KBiP_2S_6$	$K_2BaP_2S_6$
χ^{abc}/pm V^{-1}	$\chi^{112} = 1.647$	$\chi^{112} = 11.234$	$\chi^{113} = 0.171$
	$\chi^{123} = 16.114$	$\chi^{123} = 1.890$	$\chi^{333} = 0.678$
	$\chi^{222} = 67.267$	$\chi^{222} = 63.404$	—
	$\chi^{233} = 16.691$	$\chi^{233} = 0.4067$	—

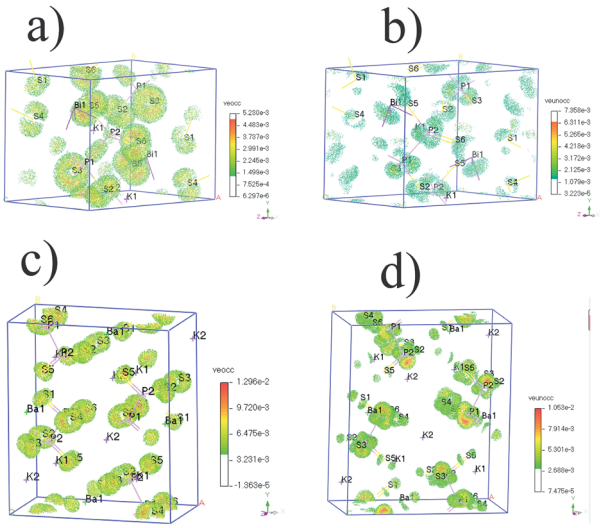

Fig. 5 (a) SHG density of VE occupied (veocc) and (b) unoccupied (veunocc) states in $KBiP_2S_6$. (c) SHG density of VE occupied (veocc) and (d) unoccupied (veunocc) states in $K_2BaP_2S_6$.

of middle IR NLO materials with a good balance of a large bandgap (4.1(1) eV), high SHG coefficient (2.1× AGS), and large LDT (8× AGS) through a mixed cation routine. From centrosymmetric $Ba_2P_2S_6$ to acentric $KSbP_2S_6$ and $KBiP_2S_6$, then finally to $K_2BaP_2S_6$, our observations demonstrate the important dual-role of mixed cations: aligning structural motifs to form NCS structures and enlarging bandgaps. Our research provides a new direction for discovering novel middle IR NLO materials. To better evaluate the properties of $(KX)P_2S_6$ (X = Sb, Bi, Ba), obtaining high quality single crystals is essential. Our initial experiments of crystal growth of $K_2BaP_2S_6$ utilizing salt flux have resulted in mm-sized crystals, which are shown in Fig. S23.† Type-I phase-matching capability, good air stability, and high SHG and LDT all indicate that $(KX)P_2S_6$ compounds (X = Sb, Bi, Ba) are excellent infrared nonlinear optical materials. The next phase for this system would be crystal growth of $(KX)P_2S_6$ compounds (X = Sb, Bi, Ba) and systemically studying their physical properties such as LDT and thermal conductivity, which are ongoing.

Conclusions

Three acentric thiophosphates $KSbP_2S_6$, $KBiP_2S_6$, and $K_2BaP_2S_6$ were synthesized *via* a high-temperature solid-state method. $KSbP_2S_6$ is isostructural to $KbiP_2S_6$, which crystallizes in the β-$KSbP_2Se_6$ structure type. $K_2BaP_2S_6$ was discovered for the first time and forms in a new structure type. $KSbP_2S_6$, $KbiP_2S_6$, and $K_2BaP_2S_6$ were predicted to be direct bandgap semiconductors. The measured bandgaps for $KSbP_2S_6$, $KBiP_2S_6$, and $K_2BaP_2S_6$ are 2.9(1) eV, 2.3(1) eV and 4.1(1) eV respectively. $KSbP_2S_6$, $KBiP_2S_6$, and $K_2BaP_2S_6$ were discovered as superior middle IR NLO materials with excellent balance between the bandgap, second harmonic generation coefficient, and laser damage threshold. The superior NLO properties of $KSbP_2S_6$, $KBiP_2S_6$, and $K_2BaP_2S_6$ originate from the comprehensive interactions

between mixed cations and $[P_2S_6]$ motifs. The mixed cations play a dual-role of aligning $[P_2S_6]$ motifs and enlarging the bandgap in $KSbP_2S_6$, $KBiP_2S_6$, and $K_2BaP_2S_6$, which is elucidated by a comprehensive study of crystal structure measurements, DFT calculations, and property tests. This study opens a new avenue for breaking the "3.5 eV wall" for middle IR NLO materials research.

Data availability

Crystallographic data for $K_2BaP_2S_6$ has been deposited at the CCDC under CCDC 2119928. The datasets supporting this article have been uploaded as part of the ESI,† DOI: 10.1039/d1sc06849k.

Author contributions

J. W. conceived the project, designed the experiments and supervised the study. V. V. and J. B. performed the experiments and analysed the data. K. W. performed the SHG test. B. Zhang performed SHG theoretical calculations. V. V., J. B., K. W., B. Zhang., and J. W. discussed the data and wrote the paper.

Conflicts of interest

There are no conflicts to declare.

Acknowledgements

This research is supported by start-up funds from Wichita State University. J. Wang thanks Arka Sarkar from Iowa State University for confirming the single crystal structure and Xiaocun Liu from Shandong University, China for help on the SEM test.

References

1 M. Yu, Y. Okawachi, A. G. Griffith, N. Picqué, M. Lipson and A. L. Gaeta, *Nat. Commun.*, 2018, **9**, 1869.
2 A. V. Muraviev, V. O. Smolski, Z. E. Loparo and K. L. Vodopyanov, *Nat. Photonics*, 2018, **12**, 209.
3 J. S. Dam, P. Tidemand-Lichtenberg and C. Pedersen, *Nat. Photonics*, 2012, **6**, 788.
4 D. Pestov, X. Wang, G. O. Ariunbold, R. K. Murawski, V. A. Sautenkov, A. Dogariu, A. V. Sokolov and M. O. Scully, *Proc. Natl. Acad. Sci. U.S.A.*, 2008, **105**, 422.
5 A. K. Majumdar and J. C. Ricklin, *Free-Space Laser Communications: Principles and Advances*, Springer Science & Business Media, New York, NY, 2010, vol. 2.
6 S.-F. Li, X.-M. Jiang, Y.-H. Fan, B.-W. Liu, H.-Y. Zeng and G.-C. Guo, *Chem. Sci.*, 2018, **9**, 5700.
7 A. Abudurusuli, J. Li and S. Pan, *Dalton Trans.*, 2021, **50**, 3155.
8 Z. Li, J. Yao and Y. Wu, *Cryst. Growth Des.*, 2020, **20**, 7550.
9 X. Chen and K. M. Ok, *Chem.–Asian J.*, 2020, **15**, 3709.
10 D. Mei, W. Cao, N. Wang, X. Jiang, J. Zhao, W. Wang, J. Dang, S. Zhang, Y. Wu, P. Rao and Z. Lin, *Mater. Horiz.*, 2021, **8**, 2330.
11 F. Liang, L. Kang, Z. Lin and Y. Wu, *Cryst. Growth Des.*, 2017, **17**, 2254.
12 I. Chung and M. G. Kanatzidis, *Chem. Mater.*, 2014, **26**, 849.
13 X. Cui, J. Xiao, Y. Wu, P. Du, R. Si, H. Yang, H. Tian, J. Li, W.-H. Zhang, D. Deng and X. Bao, *Angew. Chem., Int. Ed. Engl.*, 2016, **55**, 6708.
14 K. Wu, B. Zhang, Z. Yang and S. Pan, *J. Am. Chem. Soc.*, 2017, **139**, 14885.
15 L. Kang, M. Zhou, J. Yao, Z. Lin, Y. Wu and C. Chen, *J. Am. Chem. Soc.*, 2015, **137**, 13049.
16 C. Wu, X. Jiang, L. Lin, Y. Hu, T. Wu, Z. Lin, Z. Huang, M. G. Humphrey and C. Zhang, *Angew. Chem., Int. Ed. Engl.*, 2021, **60**, 22447.
17 H. Lan, F. Liang, X. Jiang, C. Zhang, H. Yu, Z. Lin, H. Zhang, J. Wang and Y. Wu, *J. Am. Chem. Soc.*, 2018, **140**, 4684.
18 Y.-J. Jia, Y.-G. Chen, Y. Guo, X.-F. Guan, C. Li, B. Li, M.-M. Liu and X.-M. Zhang, *Angew. Chem., Int. Ed. Engl.*, 2019, **58**, 17194.
19 X. Du, X. Guo, Z. Gao, F. Liu, F. Guo, S. Wang, H. Wang, Y. Sun and X. Tao, *Angew. Chem. Weinheim Bergstr. Ger.*, 2021, **133**, 23508.
20 G. Han, Y. Wang, X. Su, Z. Yang and S. Pan, *Sci. Rep.*, 2017, **7**, 1901.
21 B.-W. Liu, H.-Y. Zeng, X.-M. Jiang and G.-C. Guo, *CCS Chem.*, 2020, **2**, 964.
22 W. Zhou, W.-D. Yao, Q. Zhang, H. Xue and S.-P. Guo, *Inorg. Chem.*, 2021, **60**, 5198.
23 K. Wu, Y. Chu, Z. Yang and S. Pan, *Chem. Sci.*, 2019, **10**, 3963.
24 R.-A. Li, Z. Zhou, Y.-K. Lian, F. Jia, X. Jiang, M.-C. Tang, L.-M. Wu, J. Sun and L. Chen, *Angew. Chem., Int. Ed. Engl.*, 2020, **59**, 11861.
25 X. Luo, Z. Li, F. Liang, Y. Guo, Y. Wu, Z. Lin and J. Yao, *Inorg. Chem.*, 2019, **58**, 7118–7125.
26 Y.-N. Li, H. Xue and S.-P. Guo, *Inorg. Chem.*, 2020, **59**, 3546–3550.
27 H. Lin, W.-B. Wei, H. Chen, X.-T. Wu and Q.-L. Zhu, *Coord. Chem. Rev.*, 2020, **406**, 213150.
28 H. Huang, R. He, W. Yao, Z. Lin, C. Chen and Y. Zhang, *J. Cryst. Growth*, 2013, **380**, 176–181.
29 Y. Wang, B. Zhang, Z. Yang and S. Pan, *Angew. Chem., Int. Ed. Engl.*, 2018, **57**, 2150–2154.
30 H. Huang, L. Liu, S. Jin, W. Yao, Y. Zhang and C. Chen, *J. Am. Chem. Soc.*, 2013, **135**, 18319–18322.
31 S. Jörgens, A. Mewis, R.-D. Hoffmann, R. Pöttgen and B. D. Mosel, *Z. Anorg. Allg. Chem.*, 2003, **629**, 429.
32 R. D. Shannon, *Acta Crystallogr., Sect. A: Cryst. Phys., Diffr., Theor. Gen. Crystallogr.*, 1976, **32**, 751–767.
33 Q. Wei, C. He, K. Wang, X.-F. Duan, X.-T. An, J.-H. Li and G.-M. Wang, *Eur. J. Chem.*, 2021, **27**, 5880–5884.
34 M. Luo, F. Liang, X. Hao, D. Lin, B. Li, Z. Lin and N. Ye, *Chem. Mater.*, 2020, **32**, 2615–2620.
35 R. Yin, C. Hu, B.-H. Lei, S. Pan and Z. Yang, *Phys. Chem. Chem. Phys.*, 2019, **21**, 5142–5147.

36 H.-Y. Chang, S.-H. Kim, P. S. Halasyamani and K. M. Ok, *J. Am. Chem. Soc.*, 2009, **131**, 2426–2427.
37 W. Cai, Q. Jing and J. Zhang, *New J. Chem.*, 2020, **44**, 1228–1235.
38 M. Yan, H.-G. Xue and S.-P. Guo, *Cryst. Growth Des.*, 2021, **21**, 698–720.
39 *Bruker APEX2*, Bruker AXS Inc., Madison, WI, 2005.
40 G. M. Sheldrick, *Acta Crystallogr., Sect. A: Found. Crystallogr.*, 2008, **64**, 112.
41 E. Parthé and L. M. Gelato, *Acta Crystallogr., Sect. A: Found. Crystallogr.*, 1984, **40**, 169.
42 L. M. Gelato and E. Parthé, *J. Appl. Crystallogr.*, 1987, **20**, 139.
43 S. K. Kurtz and T. T. Perry, *J. Appl. Phys.*, 1968, **39**, 3798.
44 O. Jepsen, A. Burkhardt and O. K. Andersen, *The Program TB-LMTO-ASA, Version 4.7*, Max-Planck-Institut für Festkörperforschung, Stuttgart, Germany, 1999.
45 U. Barth and L. Hedin, *J. Phys. C: Solid State Phys.*, 1972, **5**, 1629.
46 B. G. Pfrommer, M. Côté, S. G. Louie and M. L. Cohen, *J. Comput. Phys.*, 1997, **131**, 233.
47 J. P. Perdew, K. Burke and M. Ernzerhof, *Phys. Rev. Lett.*, 1996, **77**, 3865.
48 A. M. Rappe, K. M. Rabe, E. Kaxiras and J. D. Joannopoulos, *Phys. Rev. B: Condens. Matter Mater. Phys.*, 1990, **41**, 1227.
49 J. D Breshears and M. G. Kanatzidis, *J. Am. Chem. Soc.*, 2000, **122**, 7839.
50 V. Manrique, A. Galdámez, D. R. León, M. T. Garland and M. Jiménez, *Z. Kristallogr. - New Cryst. Struct.*, 2003, **218**, 163.
51 B. Ji, K. Pandey, C. P. Harmer, F. Wang, K. Wu, J. Hu and J. Wang, *Inorg. Chem.*, 2021, **60**, 10603.
52 F. Menzel, W. Brockner, W. Carrillo-Cabrera, H. G. Von Schnering and Z. Anorg, *Allg. Chem.*, 1994, **620**, 1081.
53 G. Cicirello, K. Wu and B. J. Wang, *J. Solid State Chem.*, 2021, **296**, 122017.
54 X. Wu, X. Gu, H. Pan, Y. Hu and K. Wu, *Crystals*, 2018, **8**, 165.
55 L. Nian, K. Wu, G. He, Z. Yang and S. Pan, *Inorg. Chem.*, 2018, **57**, 3434.
56 Y. Guo, F. Liang, M. Zhou, Z. Lin, J. Yao and Y. Wu, *J. Alloys Compd.*, 2018, **762**, 143.
57 G. Cicirello, A. Swindle and J. Wang, *J. Solid State Chem.*, 2021, **296**, 122017.
58 J. Wang, Y. He, N. E. Mordvinova, O. I. Lebedev and K. Kovnir, *Chem*, 2018, **4**, 1465.
59 J. Wang, J.-A. Dolyniuk, E. H. Krenkel, J. L. Niedziela, M. A. Tanatar, E. I. Timmons, T. Lanigan-Atkins, H. Zhou, Y. Cheng, A. J. Ramirez-Cuesta, D. L. Schlagel, U. S. Kaluarachchi, L.-L. Wang, S. L. Bud'ko, P. C. Canfield, R. Prozorov, O. Delaire and K. Kovnir, *Chem. Mater.*, 2020, **32**, 7932.
60 J. Dünner and A. Mewis, *Z. Anorg. Allg. Chem.*, 1995, **621**, 191.
61 J. Wang, P. Yox, J. Voyles and K. Kovnir, *Cryst. Growth Des.*, 2018, **18**, 4076.
62 I. Pilchowski and A. Mewis, *Z. Anorg. Allg. Chem.*, 1990, **581**, 173.
63 J. Wang, K. Lee and K. Kovnir, *Inorg. Chem.*, 2017, **56**, 783.
64 B. Ji, E. Guderjahn, K. Wu, T. H. Syed, W. Wei, B. Zhang and J. Wang, *Phys. Chem. Chem. Phys.*, 2021, **23**, 23696.
65 N. E. Brese and M. O'Keeffe, *Acta Crystallogr., Sect. B: Struct. Sci.*, 1991, **47**, 192.
66 N. A. Moroz, C. Bauer, L. Williams, A. Olvera, J. Casamento, A. A. Page, T. P. Bailey, A. Weiland, S. S. Stoyko, E. Kioupakis, C. Uher, J. A. Aitken and P. F. P. Poudeu, *Inorg. Chem.*, 2018, **57**, 7402.
67 Z. Li, Y. Liu, S. Zhang, W. Xing, W. Yin, Z. Lin, J. Yao and Y. Wu, *Inorg. Chem.*, 2020, **59**, 7614.
68 A. Abudurusuli, K. Wu, A. Tudi, Z. Yang and S. Pan, *Chem. Commun.*, 2019, **55**, 5143.